Observational Constraint for Precipitation in Extratropical Cyclones: Sensitivity to Data Sources

CATHERINE M. NAUD

Applied Physics and Applied Mathematics, Columbia University, and Goddard Institute for Space Studies, National Aeronautics and Space Administration, New York, New York

JAMES F. BOOTH

Earth and Atmospheric Sciences, City College of the City University of New York, New York, New York

MATTHEW LEBSOCK

Jet Propulsion Laboratory, California Institute of Technology, Pasadena, California

MIRCEA GRECU

Goddard Earth Sciences Technology and Research, Morgan State University, Baltimore, and Laboratory for Atmospheres, Goddard Space Flight Center, National Aeronautics and Space Administration, Greenbelt, Maryland

(Manuscript received 12 October 2017, in final form 16 February 2018)

ABSTRACT

Using cyclone-centered compositing and a database of extratropical-cyclone locations, the distribution of precipitation frequency and rate in oceanic extratropical cyclones is analyzed using satellite-derived datasets. The distribution of precipitation rates retrieved using two new datasets, the Global Precipitation Measurement radar–microwave radiometer combined product (GPM-CMB) and the Integrated Multisatellite Retrievals for GPM product (IMERG), is compared with *CloudSat*, and the differences are discussed. For reference, the composites of AMSR-E, GPCP, and two reanalyses are also examined. Cyclone-centered precipitation rates are found to be the largest with the IMERG and *CloudSat* datasets and lowest with GPM-CMB. A series of tests is conducted to determine the roles of swath width, swath location, sampling frequency, season, and epoch. In all cases, these effects are less than $\sim$0.14 mm h^{-1} at 50-km resolution. Larger differences in the composites are related to retrieval biases, such as ground-clutter contamination in GPM-CMB and radar saturation in *CloudSat*. Overall the IMERG product reports precipitation more often, with larger precipitation rates at the center of the cyclones, in conditions of high precipitable water (PW). The *CloudSat* product tends to report more precipitation in conditions of dry or moderate PW. The GPM-CMB product tends to systematically report lower precipitation rates than the other two datasets. This intercomparison provides 1) modelers with an observational uncertainty and range (0.21–0.36 mm h^{-1} near the cyclone centers) when using composites of precipitation for model evaluation and 2) retrieval-algorithm developers with a categorical analysis of the sensitivity of the products to PW.

1. Introduction

Precipitation in the midlatitudes is important to society as a water source and through its association with extreme events. Extratropical cyclones play a dominant role in precipitation at these latitudes, contributing up to 90% of the total precipitation in the Northern Hemisphere (NH) winter (Hawcroft et al. 2012; Catto et al. 2012). There are still issues in the representation of midlatitude precipitation in current general circulation models (GCMs; e.g., Stephens et al. 2010; Catto et al. 2015; Hawcroft et al. 2016); to assess this representation,

Corresponding author: Catherine M. Naud, cn2140@columbia.edu

DOI: 10.1175/JAMC-D-17-0289.1

an observational benchmark and a measure of observational uncertainty are needed.

In the recent past, the NASA–JAXA Tropical Rainfall Measuring Mission (TRMM; Simpson et al. 1988; Kummerow et al. 1998, 2000) has been one of the primary sources of satellite observations of precipitation, but these observations are limited by the latitude range sampled by the instrument (50°N–50°S at most). Offering better latitudinal coverage, observations from the Advanced Microwave Scanning Radiometer for the Earth Observing System (AMSR-E; Kawanishi et al. 2003) are also used over the oceans (Kummerow et al. 2011), but this instrument has some sensitivity issues in the midlatitudes (Stephens et al. 2010; Behrangi et al. 2012). The availability of gridded combined products such as the Global Precipitation Climatology Project (GPCP; Adler et al. 2003) helps to overcome the coverage issue, but these are typically daily datasets and do not provide a fine temporal match with extratropical cyclones. Global and gridded reanalysis products of precipitation can also be used, but their accuracy is still under examination (e.g., de Leeuw et al. 2015; Reichle et al. 2017).

With the launch of the Global Precipitation Measurement (GPM; Hou et al. 2014) *Core Observatory* satellite in 2014, a new source of precipitation information has become available that includes both microwave and radar information to obtain a better precipitation retrieval in conditions of light rain or frozen hydrometeors for a wide latitude range up to 65°N–65°S (Skofronick-Jackson et al. 2017). The objective of this paper is to explore the differences in extratropical-cyclone-centered composites of surface precipitation rates between the new datasets offered by the GPM mission and other observation-based data sources.

Cyclone-centered compositing of satellite observations is an effective method for model evaluation, as demonstrated in previous analyses of clouds, cyclone thermodynamics, dynamics, precipitation, and water vapor (e.g., Lau and Crane 1995; Klein and Jakob 1999; Bauer and Del Genio 2006; Naud et al. 2006, 2010; Field and Wood 2007; Field et al. 2008, 2011; Catto et al. 2010; Rudeva and Gulev 2011; Hawcroft et al. 2012, 2016; Govekar et al. 2014). Compositing uses the center of the extratropical cyclones as an anchor for averaging multiple systems together. As such, the resulting composite provides a representation of the most salient features that all of these systems have in common and reduces much of the natural variability so that comparisons can be made with modeled cyclones that are not coincident or collocated with observations. For precipitation, these composites have been used for model evaluation in various studies (e.g., Bauer and Del Genio 2006; Catto et al. 2015; Field et al. 2008, 2011; Hawcroft et al. 2016), using disparate precipitation datasets for reference. It is thus important to compare new and older sources of precipitation information and also to characterize issues in the composites caused by observational uncertainties.

In this analysis, the recent products to be examined are the combined radar–radiometer product from the GPM *Core Observatory* mission (GPM-CMB; Grecu et al. 2016), the Integrated Multisatellite Retrievals for GPM gridded product (IMERG; Huffman et al. 2017), and the *CloudSat* level-2C precipitation column (2C-PRECIP-COLUMN; Haynes et al. 2009). The *CloudSat* instrument (Stephens et al. 2002) has been found to be very accurate in the midlatitudes because of its ability to detect light precipitation (Haynes et al. 2009; Behrangi et al. 2012). So far, two major issues for compositing *CloudSat* were its narrow swath and its sporadic sampling, but the now mostly continuous 10-yr period of operation allows much better data sampling than before. In addition, other sources explored here for reference to previous work are the AMSR-E precipitation product (Kummerow et al. 2011), the GPCP One-Degree Daily precipitation product (GPCP-1DD; Huffman et al. 2001), and precipitation from two reanalyses: the European Centre for Medium-Range Weather Forecasts interim reanalysis (ERA-Interim; Dee et al. 2011) and the Modern-Era Retrospective Analysis for Research and Applications, version 2 (MERRA-2; Gelaro et al. 2017).

The aim of this study is not to search for the best product but instead to diagnose specific characteristics of the datasets for extratropical-cyclone precipitation so as to 1) inform modelers on which product might be best for their applications and 2) assist in refinement of the retrieval and/or blending algorithms for the newer datasets. As such, the goals are to compare recent datasets as well as existing, more extensively used, datasets and to quantify the observational variability in extratropical-cyclone composites across the datasets. The analysis described herein focuses on an intercomparison of cyclone-centered composites of surface precipitation obtained for both the NH and Southern Hemisphere (SH) 30°–60° latitude bands over the oceans. We discuss the impact of observational uncertainties and sampling-related issues as well as explore the sensitivity of precipitation in extratropical cyclones to environmental moisture amount and its implication for seasonal variations according to the three recent datasets: GPM-CMB, IMERG, and *CloudSat*.

2. Data sources

In this study we explore precipitation rates obtained from different observational products: GPM-CMB, IMERG,

TABLE 1. Summary of all of the precipitation products used in this analysis, with name, characteristics (instrument, resolution, and version), period of data collection for the analysis, and reference.

Product	Characteristics	Period	Reference
GPM-CMB	Combined radar and radiometer product; Ku + GMI (245-km swath width; 5-km resolution) and Ka + Ku + GMI (120-km swath width; 5-km resolution); version 5	2014–16	Grecu et al. (2016)
IMERG	Multiplatform radiometers; global gridded 0.1° spatial and 30-min temporal resolutions; version 4	2014–16	Huffman et al. (2017)
CloudSat PRECIP-COLUMN	W band; 1.4 km × 1.7 km footprint; release 4	2006–16	Haynes et al. (2009)
AMSR-E	Microwave radiometer; swath width 1450 km and spatial resolution 5.4 km; version 10	2006–10	Kummerow et al. (2011)
GPCP-1DD	Multiple platform; 3-hourly satellites, daily rain gauges, and gridded product of 1° spatial and daily temporal resolutions; version 1.2	2006–15	Huffman et al. (2001)
ERA-Interim	Reanalysis; 1.5° × 1.5° spatial and 6-hourly temporal resolutions	2006–16	Dee et al. (2011)
MERRA-2	Reanalysis; 0.5° × 0.67° spatial and 3-hourly temporal resolutions	2006–16	Gelaro et al. (2017)

CloudSat, AMSR-E, and GPCP-1DD. Table 1 provides a list of these products and their associated characteristics. We focus on midlatitude regions between 30° and 60° for both hemispheres, for all seasons. The time period of focus is 2014–16; a different range of years is used for some of the datasets on the basis of data availability. The impact of differing epochs on the results will be discussed later.

The GPM *Core Observatory* was launched in February of 2014 to a non-sun-synchronous orbit spanning 65°S–65°N and has been continuously operating and delivering data since March of that year. A full description of the platform, instruments, products, and algorithms is given in Skofronick-Jackson et al. (2017). The platform hosts the GPM Microwave Imager (GMI) instrument as well as two radars: one Ka band (KaPR; 35.5 GHz) and one Ku band (KuPR; 13.6 GHz), jointly called the Dual-Frequency Precipitation Radar (DPR). The dataset used here is version 5 of the CMB (Grecu et al. 2016), and we will test two versions of the product: the combination of KuPR and GMI (Ku + GMI) and the combination of KaPR, KuPR, and GMI (Ka + Ku + GMI). These products provide 5-km-resolution precipitation rate and type in a 245-km swath for Ku + GMI and a 125-km swath for Ka + Ku + GMI. Grecu et al. (2016) describe the algorithm and present some preliminary evaluations: over the midlatitude oceans, they find larger rainfall estimates when using Ka + Ku + GMI than when using Ku + GMI. This is most likely because the inclusion of the Ka-band radar observations allows for more accurate estimates of the precipitation particle size distributions. Because of its relative novelty, to our knowledge these retrievals have not been used yet to explore precipitation in oceanic extratropical cyclones. We will refer to this product as GPM-CMB.

As part of the same mission, the IMERG (Huffman et al. 2017) product is a global, gridded, merged precipitation dataset, with 0.1° and 30-min spatial and temporal resolutions. After applying a Goddard profiling (GPROF)–like algorithm (Kummerow et al. 2015) to multiple sensors that are part of the GPM constellation, the product merges and grids these microwave precipitation estimates with microwave-calibrated infrared satellite estimates and precipitation gauge analysis for the GPM era while applying an intercalibration procedure, a gauge adjustment, and schemes to fill in the gaps (Skofronick-Jackson et al. 2017). The intercalibration of the radiometers is performed using the precipitation estimates of the combined GMI–DPR product. The files used in this study were processed as part of the latest version-4 processing "research/final run" sequence for 2014–16. This dataset is of particular importance for model-evaluation purposes because of its global nature, as well as its high spatial and temporal resolutions. In addition, daily and monthly versions are available. Here we also examine the daily product.

As part of the "A-Train," two instruments have the capability to observe and characterize precipitation and have been extensively used for this purpose in the midlatitudes: the AMSR-E on *Aqua* and the W-band *CloudSat* radar. The AMSR-E period of operation was 2002–11, and here we use data from 2006 to 2010. The retrieval relies on brightness temperatures measured in the microwave spectrum that have been trained on coincident radar observations from the TRMM Precipitation Radar. A detailed description of the retrieval algorithm is available in Kummerow et al. (2011). Here we use a fairly dated version of the product, version 10, in an effort to match earlier studies that used this dataset (e.g., Field and Wood 2007; Field et al. 2011).

We also collected precipitation retrievals from the version-4 release of the 2C-PRECIP-COLUMN product of *CloudSat* (Haynes et al. 2009) for the period 2006–16. Of all the datasets explored here, this one is the most sensitive to light precipitation (e.g., Stephens et al.

2010) because of the radar frequency (W band; 94 GHz). The 2C-PRECIP-COLUMN product uses the two-way path-integrated attenuation of the radar beam and the height of the precipitating column to estimate the rain rate. One drawback is that total attenuation (above roughly 60 dB) can occur in heavy-precipitation events, causing underestimates in the surface precipitation rate. Because retrievals can still be made when attenuation occurs, to alert the users to potential attenuation errors, precipitation-rate retrievals are flagged in the product (the retrieved precipitation rates are reported as negative numbers). Here, unless otherwise stated, we keep these retrievals (using the absolute value). This product is only available along the nadir track of the radar, and so the swath width is only about 1.4 km, the single-footprint width (Tanelli et al. 2008).

Another gridded global dataset is the GPCP-1DD product, which has been extensively used to evaluate GCMs (e.g., Hawcroft et al. 2012). This dataset provides daily precipitation at 1° spatial resolution from a combination of monthly rain gauge analyses and 3-hourly satellite observations (Huffman et al. 2001). We use here data from version 1.2 for the period of 2006–15.

Reanalyses are also often used to provide precipitation for model evaluation. Here we compare the MERRA-2 and ERA-Interim reanalyses with the observational datasets. MERRA-2 is available at a 3-hourly 0.5° × 0.67° resolution; ERA-Interim is 6 hourly, and we use data that have been provided at a 1.5° × 1.5° resolution. Finer-resolution ERA-Interim products are available, but we chose this resolution because it is similar to that of GCMs. For both reanalyses, we considered data for the period of 2006–16.

3. Method

Our compositing method involves three steps: 1) associate precipitation information to a cyclone, 2) project this information into an equal-area rectangular 50-km-resolution grid centered on the sea level pressure minimum (i.e., the cyclone center), and 3) average precipitation rates over all cyclones available for each dataset by superimposing all 50-km grid cells using the cyclone center as the anchor. To average cyclones from the SH with those of the NH, we flip the SH cyclones to place the polar side of the cyclones at the top of the grids.

The cyclones are located using the Modeling, Analysis, and Prediction program Climatology of Mid-Latitude Storm Area (MCMS) algorithm (Bauer and Del Genio 2006; Bauer et al. 2016), which provides cyclone locations and tracks obtained using 6-hourly ERA-Interim sea level pressure. For this study, we consider each 6-hourly cyclone identification as independent from other identifications of the same system at different times.

Steps 1 and 2 are illustrated in Fig. 1 for the GPM-CMB product. For the precipitation products that are available as instantaneous data along a narrow-swath orbit (i.e., GPM-CMB, AMSR-E, and *CloudSat*), we extract the segment of orbit that is found within 2500 km of the cyclone center, in a time period of ±3 h around the time of cyclone identification. Figure 1a shows an example for Ku + GMI orbits that match these criteria. For the gridded products, we extract all grid cells in the 2500-km radius region: for IMERG we collect all 30-min data files within ±3 h of the cyclone detection, and MERRA-2 and ERA-Interim are matched in time with the cyclones. For GPCP-1DD and IMERG Daily, we match the precipitation information to cyclones identified at 1200 UTC.

Then we apply the same gridding algorithm to all of these data sources: we construct a rectangular grid of 50-km resolution and dimension ±1500 km in the north–south and east–west directions, centered on the cyclone minimum in sea level pressure. Each grid cell is defined on the basis of the distance between its center and the center of the cyclone. For each dataset to be composited, the data points are allocated into each grid cell on the basis of their distance in kilometers to the center of the cyclone. Each grid cell has the same area (50 km × 50 km). Figure 1b shows the projected GPM Ku + GMI precipitation rates for the example of Fig. 1a. For each cyclone, grid cells that are encompassed by the sensors' swath contain the accumulated precipitation and the number of data points that contribute to it. For the reanalyses that have a resolution close or lower than the 50-km resolution chosen here, the 50-km-resolution grid cells contain the precipitation from the closest grid cell in the reanalysis output.

We thus obtain databases of cyclones with precipitation information for each of the data sources. Of the 50 000 six-hourly cyclone snapshots identified in both NH and SH oceans in the 2014–16 period, about 36 000 cyclones (i.e., 6-hourly snapshots) are associated to GPM Ku + GMI precipitation retrievals. Because of the wider Ku + GMI coverage, more precipitation retrievals will be available per cyclone with this product than with *CloudSat* or Ka + Ku + GMI. For the full 2006–16 period, of the 190 000 identified cyclones (6-hourly snapshots), about 110 000 have *CloudSat* precipitation retrievals associated with them.

Although the cyclone centers are selected when they are found over the oceans, the entire cyclone area might include land or sea ice. Products such as IMERG provide precipitation rates over land as well as oceans, but we found no noticeable impact of land or sea ice contamination in the IMERG precipitation composites (not shown).

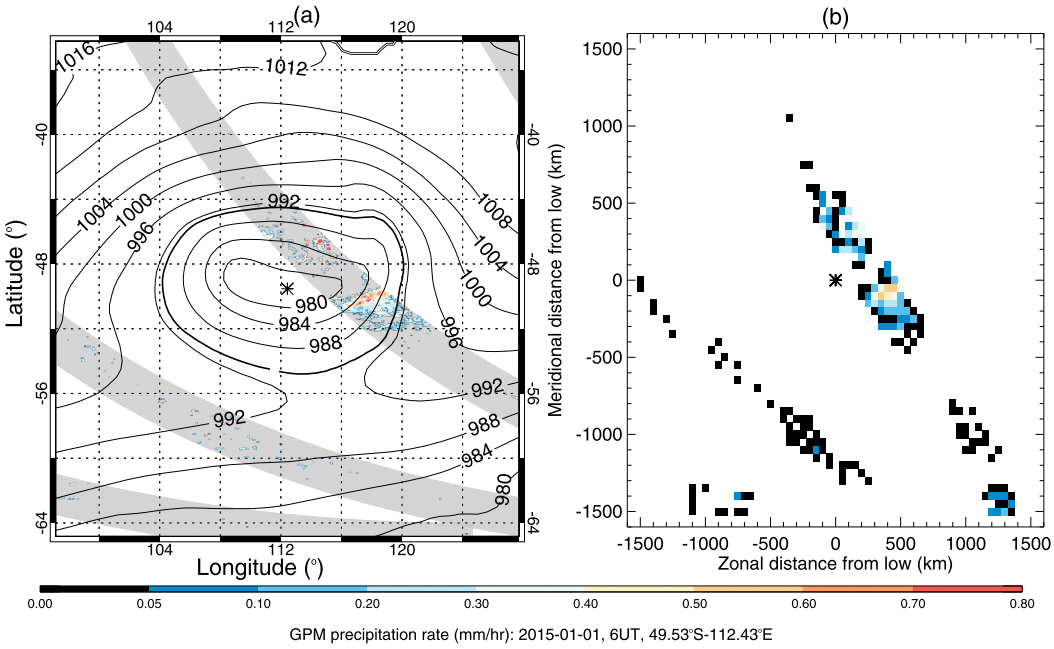

FIG. 1. Example of an extratropical cyclone located at 49.53°S, 112.43°E at 0600 UTC 1 Jan 2015: (a) GPM Ku + GMI orbits with precipitation rate located in close proximity to the storm center within ±3 h of cyclone detection. The solid lines show the MERRA-2 sea level pressure contours. (b) The corresponding GPM precipitation rates projected on a 50-km-resolution equal-area grid centered on the cyclone low pressure point (asterisk).

4. Results

For all of the observational datasets presented above, we calculate composites of mean precipitation rates by averaging all of the cyclone-centered retrievals whether or not they detect precipitation. Although the resolution of the precipitation retrievals differs among datasets, we find that they all have a minimum precipitation rate on the order of 10^{-4} mm h^{-1} at the 50-km-resolution scale chosen here. To provide a more quantitative characterization of the different datasets, Table 2 contains the means obtained in two areas defined about the extratropical-cyclone (ETC) centers: a 1000×1000 km^2 area and the larger 3000×3000 km^2 domain for each of the composites and various tests presented below.

a. *Cyclone-centered total precipitation*

Figure 2 shows the cyclone-centered composites of precipitation for the level-2 (instantaneous) products (AMSR-E, GPM-CMB, and *CloudSat*), and Fig. 3 shows the same for the global gridded products (IMERG and GPCP-1DD). In both figures, the cyclone-centered composites of precipitation all share similar features, consistent with previous studies (e.g., Bauer and Del Genio 2006; Field and Wood 2007; Naud et al. 2006, 2012): a comma-shaped area of relatively large precipitation that wraps around the low pressure center with a tail expanding into the warm sector, a maximum near the storm center into the warm-frontal region (northeast of the low pressure center in the NH and southeast of it in the SH), and a region of relatively light precipitation on the polar side of the low, in the western quadrant. The shape of this pattern is more representative of a probability map for precipitation than it is representative of any single cyclone, because many storms have precipitation constrained to smaller frontal regions. It does, however, offer a very useful metric for comparing observations that have different spatial footprint sizes. Here we use it to explore composite rain-rate differences, but for ease and clarity in presentation we refer to the rain rates in the same manner that we use with individual storms.

Figure 2 reveals differences among the different datasets: at the center, in the region of relative maximum precipitation, AMSR-E shows the lowest rates and *CloudSat* shows the largest. GPM-CMB Ku + GMI shows lower rates than Ka + Ku + GMI, in agreement with the Grecu et al. (2016) assessment. For *CloudSat*, the area with precipitation above 0.1 mm h^{-1} is more widespread as are the areas at weaker precipitation thresholds. This is most likely because of its very good detection sensitivity. Notably though, *CloudSat* has a higher mean rate throughout the cyclone composite,

TABLE 2. Cyclone-centered mean within ±500 km and ±1500 km of cyclone center of precipitation and precipitation distribution.

Parameter	Dataset	±500 km	±1500 km
Total precipitation (mm h^{-1})	ERA-Interim	0.31	0.14
	MERRA-2	0.28	0.14
	2014–16	0.30	0.14
	2010–12	0.28	0.14
	GPM ETCs	0.30	0.14
	CloudSat ETCs	0.28	0.14
	GPM pixels	0.27	0.14
	CloudSat pixels	0.26	0.13
	AMSR-E	0.15	0.08
	GPM-CMB Ku + GMI	0.19	0.09
	GPM-CMB Ka + Ku + GMI	0.21	0.10
	CloudSat	0.36	0.17
	IMERG	0.34	0.15
	IMERG Daily (×24)	0.30	0.15
	GPCP (×24)	0.20	0.13
Percentage of pixels: No precipitation	IMERG	51%	68%
	GPM-CMB	60%	73%
	CloudSat	58%	70%
Percentage of pixels: Light precipitation	IMERG	16%	13%
	GPM-CMB	13%	11%
	CloudSat	13%	12%
Percentage of pixels: Moderate precipitation	IMERG	24%	14%
	GPM-CMB	21%	13%
	CloudSat	19%	13%
Percentage of pixels: Heavy precipitation	IMERG	8%	4%
	GPM-CMB	6%	3%
	CloudSat	10%	5%
Total precipitation for low PW	IMERG	0.10	0.08
	GPM-CMB	0.11	0.09
	CloudSat	0.17	0.15
Total precipitation for medium PW	IMERG	0.32	0.15
	GPM-CMB	0.28	0.12
	CloudSat	0.50	0.21
Total precipitation for large PW	IMERG	0.52	0.19
	GPM-CMB	0.34	013
	CloudSat	0.36	0.15

including the areas of heaviest precipitation where total attenuation is expected.

Figure 3a shows that the 30-min IMERG composite agrees closely with *CloudSat* (Fig. 2c), with a similarly large maximum value at the center. The area of relative minimum shows lower rates in IMERG. Use of IMERG Daily means and the 1200 UTC cyclones in the composite leads to lower precipitation rates than when using instantaneous values and the four possible times of cyclone identification (Fig. 3b). Nevertheless, the IMERG Daily composite precipitation (Fig. 3b) is overall stronger than GPCP-1DD precipitation (Fig. 3c) over the warm-frontal region and warm sector while showing lower values in areas poleward and west of the low. Despite using a similar algorithm suite, there are steps specific to IMERG and not included in the GPCP-1DD algorithm that might explain some of the differences, such as the use of the DPR–GMI combined estimates for the intercalibration of the different radiometers utilized in the IMERG production. Other potential causes for difference are the differing spatial resolutions and temporal sampling of the observations. This being said, these differences between GPCP-1DD and IMERG cyclone composites are consistent with the Behrangi et al. (2014) assessment of GPCP-1DD when compared with their multiplatform precipitation product, that is, a tendency for GPCP-1DD to underestimate precipitation at lower latitudes where precipitation is relatively large (as in the center of the cyclones) and to overestimate at higher latitudes where precipitation is relatively light (as in the area away from the cyclone center).

We construct similar composites using surface precipitation from the two reanalyses (Fig. 4). Both reanalyses give a spatial distribution that is similar to that of the observations. The maximum precipitation near the center is greater than Ka + Ku + GMI and less than

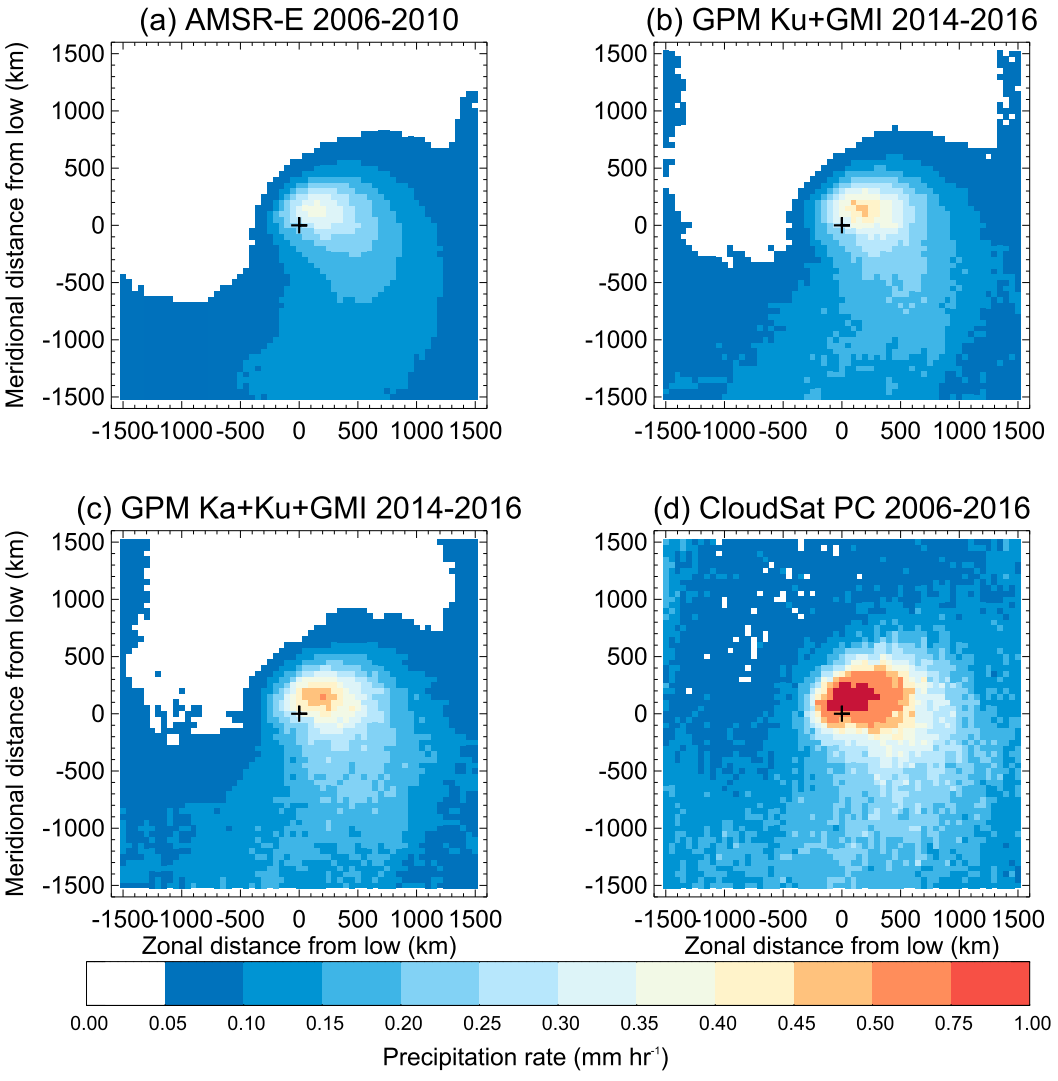

FIG. 2. Cyclone-centered composites of precipitation (rates $\geq 0\,\text{mm h}^{-1}$) obtained with (a) AMSR-E for 2006–10, (b) GPM Ku + GMI for 2014–16, (c) GPM Ka + Ku + GMI for 2014–16, and (d) *CloudSat* PRECIP-COLUMN for 2006–16.

IMERG, whereas the relative minimum in the western-poleward quadrant is similar to *CloudSat* or GPCP-1DD and thus larger than that of IMERG or either GPM product. Because its resolution is coarser than the 50-km resolution that we chose for the cyclone-centered grids, the ERA-Interim composite shows some striping. For composites that are based on a 150-km grid (not shown), the striping disappears but the precipitation distribution remains unchanged.

b. *Uncertainties caused by differing sensitivity to precipitation rates*

The compositing analysis of the level-2 and level-3 products and reanalyses provides a range of precipitation values that could be useful for a model evaluation, but it is difficult to determine which of these composites are more accurate than the others. On the basis of known strengths and limitations of the instruments, we can add information that would be useful to modelers when using these composites and would help them to decide which product would be more accurate for their application. To examine the impact of these inherent strengths and weaknesses, we focus on GPM-CMB Ka + Ku + GMI (hereinafter simply GPM-CMB), *CloudSat*, and IMERG and explore the distribution of precipitation rates in the cyclones for all three datasets. For this we count the number of 50-km grid cells, across all cyclones, that fall into each of the following arbitrarily defined precipitation-rate bins: $0\,\text{mm h}^{-1}$ (no precipitation), 10^{-4}–$0.05\,\text{mm h}^{-1}$ (light precipitation),

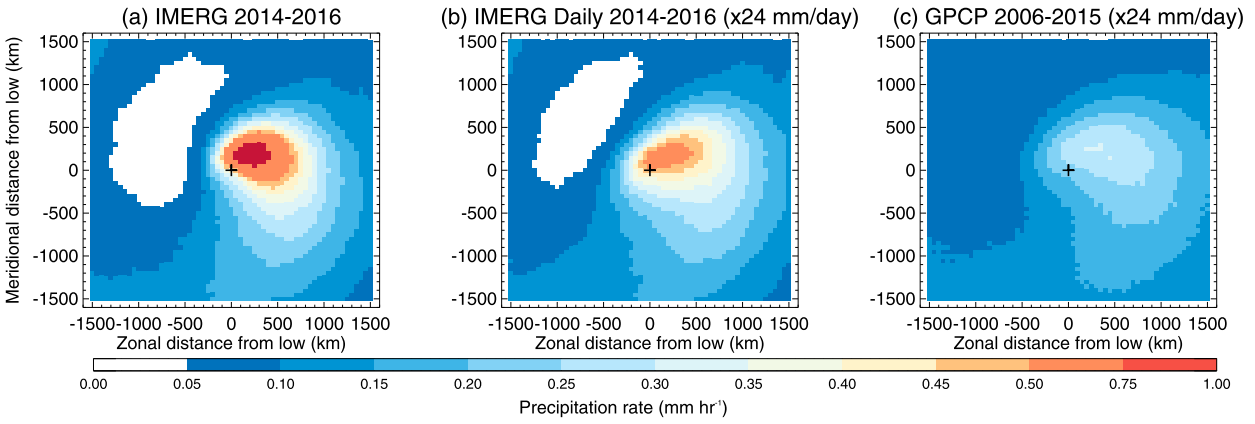

FIG. 3. As in Fig. 2, but for the gridded product: (a) IMERG 30 min for 2014–16, (b) IMERG Daily for 2014–16, and (c) GPCP-1DD for 2006–15. The two daily products are divided by 24 to match the color scale, which is in millimeters per hour.

0.05–1 mm h^{-1} (moderate precipitation), and >1 mm h^{-1} (heavy precipitation).

To compare the three datasets, we need to ensure that these categories are not dependent on each dataset's resolution. This is because the frequency of occurrence of precipitation changes with resolution (Stephens et al. 2010). Matching *CloudSat*'s one-dimensional sampling with IMERG two-dimensional product is not a trivial exercise. We need to define the length of a segment along the *CloudSat* track that would best represent the area covered by IMERG. This length should be between the actual size of an IMERG pixel (~10 km) and the length that would provide the same 10 km × 10 km area. Behrangi et al. (2012) used both a linear chord length and an area-matching estimate to obtain a lower and upper bound of *CloudSat* precipitation frequency. Stephens et al. (2010) used TRMM data to obtain a 3:1 ratio (vs 4:1 ratio to ensure equal area) to compare *CloudSat* frequencies with gridded climate-model output. Here, after a series of tests using the linear chord (6 footprints), the 3:1 ratio of Stephens et al. (2010; 18 footprints) and the area-matching condition (42 footprints), we decided to impose the equal-area criterion. So we first average the *CloudSat* precipitation in 42 footprints (42 × 1.4 × 1.7 = 99.96 km^2) to match the approximately 10 km × 10 km (100 km^2) IMERG resolution before building the 50-km-resolution cyclone-centered *CloudSat* gridded product. For the GPM-CMB product, we regrid using 2 × 2 pixel averages to match the 100-km^2 area.

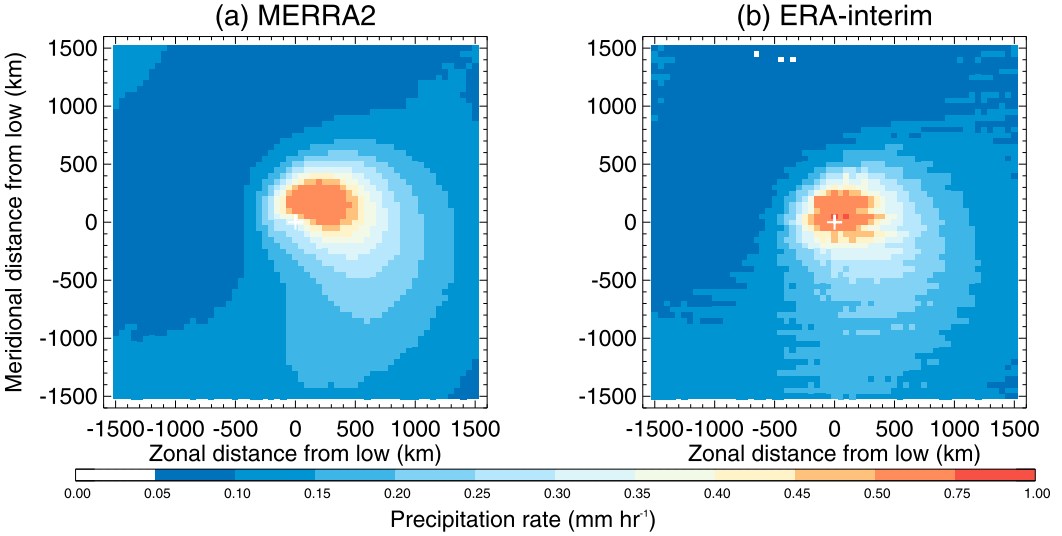

FIG. 4. As in Fig. 2, but for (a) MERRA-2 and (b) ERA-Interim precipitation composites.

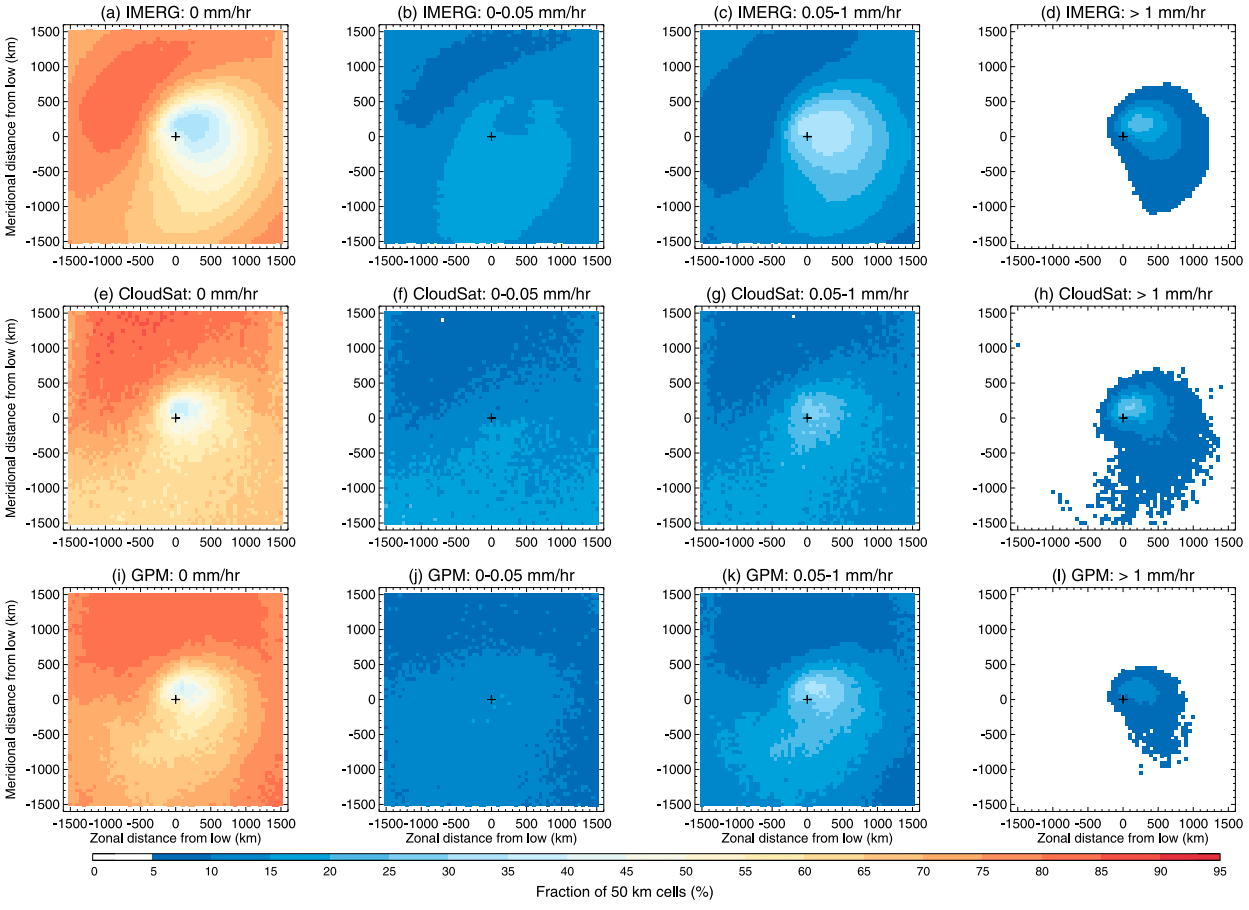

FIG. 5. Cyclone-centered composites of the percentage of 50-km cells with precipitation rates in four different ranges for three datasets: (a)–(d) IMERG, (e)–(h) *CloudSat* 36 pixels, and (i)–(l) GPM-CMB Ka+Ku + GMI 4 pixels for the ranges (left) 0, (left center) 0–0.05, (right center) 0.05–1, and (right) greater than 1 mm h^{-1}.

Figure 5 demonstrates the overall distribution of precipitation rates in the cyclone region:

1) Precipitation-free areas (Figs. 5a,e,i) are most often found in the cold sector, especially in the western quadrant on the polar side of the low. This relatively colder and drier area of the cyclones displays very little precipitation over the oceans, regardless of which platform is used for the retrievals. The area close to and slightly east of the center shows a relative minimum in zero precipitation fraction, but even there zero precipitation is still found close to 25%–30% of the time. This figure illustrates the effect of compositing with respect to what the distribution of precipitation in an individual cyclone might be.
2) Light precipitation rates (Figs. 5b,f,j) occur more often on the equatorward side of the low pressure center, with a maximum slightly to the west, more or less corresponding to the area behind the cold fronts.
3) Moderate precipitation rates (Figs. 5c,g,k) occur principally near the cyclone center and warm-frontal zone but also tail into the warm sector.
4) Heavy precipitation rates occur (Figs. 5d,h,l) most frequently in the area just poleward and east of the center, again corresponding to the warm-frontal region, with some occurrences also found in the warm sector.

This figure demonstrates the high variability of precipitation occurrence in these systems, in part because these composites are not anchored to the warm- or cold-frontal locations where precipitation would be occurring most often. It also indicates that 1) precipitation in the cold sector of oceanic cyclones is rare, 2) light precipitation occurs mostly on the equator side of the low, on both sides of the cold fronts, and 3) heavy precipitation is (not surprisingly) observed in the warm conveyor belt (e.g., Field and Wood 2007).

All three products agree to first order with the relative locations of the rain-rate categories. There are some differences as well:

1) In the warm sector IMERG reports light and moderate precipitation more often than the other two datasets, or it could be said that IMERG reports zero precipitation less often than do the other two datasets. This result might be caused by the differences in resolution despite our efforts, or it might reveal a tendency for the microwave radiometers to report false detections more often than radars.
2) In the post-cold-frontal region (western-equatorward quadrant, at least 750 km away from the low pressure center), *CloudSat* reports slightly more (~+5%) of the light precipitation, but to some degree this is dependent on the number of footprints chosen to match IMERG's resolution.
3) IMERG and *CloudSat* tend to agree on the frequency of occurrence of heavy precipitation, whereas GPM-CMB tends to estimate higher rates less often.
4) GPM-CMB and IMERG detect moderate rain rates more often than *CloudSat.*
5) GPM-CMB detects zero precipitation more often and light precipitation less often than the other two datasets, suggesting lower sensitivity to light precipitation with low radar reflectivity.

These results for GPM-CMB are consistent with the findings of Casella et al. (2017) who, on the basis of the evaluation of coincident *CloudSat* and GPM DPR observations, estimated that the DPR misses more than 90% of the snow radar echoes detected by *CloudSat*. This may affect DPR's ability to detect precipitation even when the phase at the surface is rain because, as a result of ground clutter, the lowest clutter-free DPR observations might be associated with snow. Indeed, composites of precipitation liquid fraction obtained with GPM-CMB and *CloudSat* disagree: whereas *CloudSat* detects 96% liquid fraction at least at the surface in the cyclones, the liquid fraction can be as low as 30% in the GPM-CMB retrievals (not shown). Because of this issue, one would expect GPM-CMB to report precipitation less often than *CloudSat*. For *CloudSat*, the results are also consistent with the saturation issue mentioned earlier, which might explain the lower frequency of moderate precipitation for *CloudSat* relative to the other two datasets. To illustrate this, Fig. 6 shows where the radar attenuation occurs across all cyclones in the database and indicates a maximum occurrence of approximately 10% in the area where moderate precipitation and heavy precipitation occur, suggesting that this issue probably affects both the 0.05–1 and >1 mm h^{-1} categories.

These differences in distribution across the three datasets might also be largely influenced by the difference

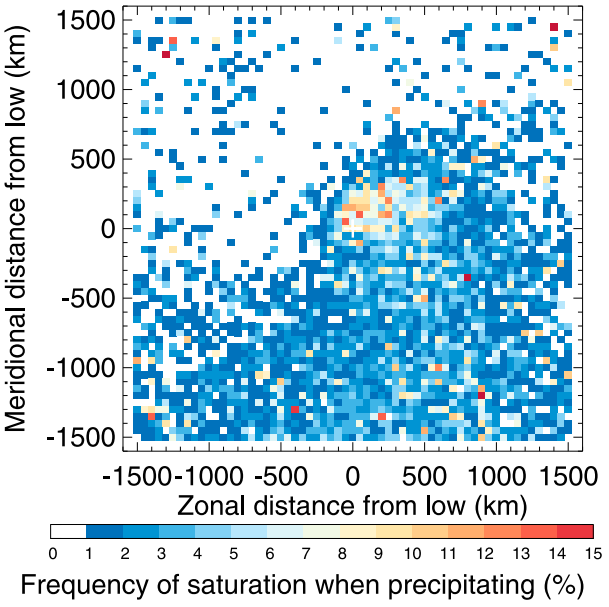

FIG. 6. Cyclone-centered composite of the frequency of occurrence of attenuated pixels in the *CloudSat* precipitation dataset.

in cyclone properties and sampling. So before we can draw any conclusions as to the impact of differing instrument/retrieval accuracies on the composite differences, we explore the impact of sampling.

c. *Uncertainties caused by differences in sampling of the cyclones*

All three datasets cover different periods of time, sample each cyclone with differing coverage, and do not sample the same number of cyclones. Here we examine the impact of these differences on the composites. To do so, we use the MERRA-2 surface precipitation because 1) it is global and 2) it covers a longer period than IMERG does. We sample MERRA-2 precipitation as if it were observed by either one of the GPM or *CloudSat* platforms by selecting MERRA-2 grid cells along their respective swaths.

The first test is to establish the effect of interannual variability on the precipitation composites, and we compare the composite of MERRA-2 precipitation obtained for 2014–16 with the one obtained for the full 2006–16 period. Figure 7a indicates that the largest difference in composite between these two periods is found in the area near the center of maximum precipitation. It also reveals that this difference is less than 0.06 mm h^{-1}. Because this difference could be caused by the differing length of the two periods and associated difference in sample size, we also compare the MERRA-2 composites obtained for 2010–12 with 2014–16. Figure 7b shows a difference in MERRA-2 composite of a similar

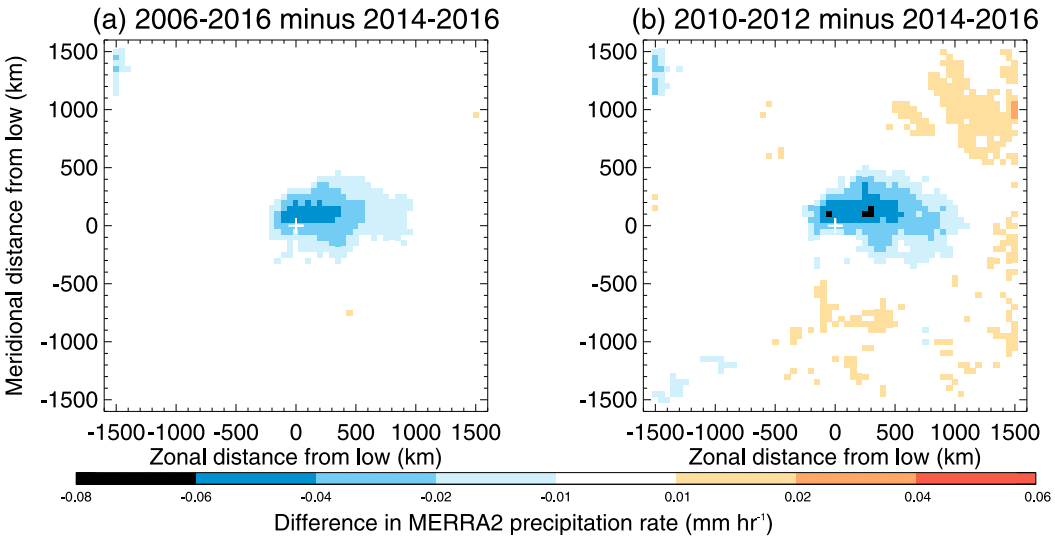

FIG. 7. Difference in cyclone-centered MERRA-2 precipitation composite (a) between the mean over 2006–16 and the mean over 2014–16 and (b) between the mean over 2010–12 and the mean over 2014–16.

magnitude, suggesting that the difference obtained in Fig. 7a has more to do with the choice of 2014–16 than the duration of the period. These two plots suggest that GPM-CMB and IMERG could be slightly overestimating near the center relative to other datasets because of the period that they cover. Such epochal variations are relevant when comparing these observed datasets with a free-running GCM, for example.

The second test is designed to determine whether the subset of cyclones that are actually observed by GPM-CMB and *CloudSat* is representative of the full cyclone population for the period of time over which these two instruments have been operating. About 2/3 and 1/2 of the cyclones are actually sampled by GPM-CMB and *CloudSat*, respectively. Figures 8a and 8c show the difference in MERRA-2 precipitation composites when these are obtained for the full database for each instrument period and those cyclones actually sampled by GPM-CMB and *CloudSat*, respectively. These two panels show very small differences—less than $0.04\,\mathrm{mm\,h^{-1}}$, suggesting that this "subset" issue has little impact on the cyclone composites. This result means that comparing observations with a free-running GCM output should not be affected by the mismatch between real and simulated cyclones.

The third test is related to the fact that, because of their narrow swath (in particular, that of *CloudSat*), only small portions of the cyclones are actually observed by GPM-CMB and *CloudSat*. Figures 8b and 8d show the difference in MERRA-2 composites when the entire area is sampled and included in the average versus when only a few narrow swaths are included (e.g., Fig. 1). In this case, the differences are much larger and can reach $0.14\,\mathrm{mm\,h^{-1}}$ close to the center and in the warm sector. Consequently, for a difference between modeled and observed precipitation to be of any significance, it would have to be larger than this $0.14\,\mathrm{mm\,h^{-1}}$ near the center, although less so in the warm sector.

Another possible cause for differences in the composites is the properties of the cyclones themselves, which might differ among the datasets. So here we test the distribution of the cyclone populations in each dataset in terms of their age, location, and the time of year in which they are detected. Figure 9 shows how the cyclones are distributed for each dataset as a function of time to peak (6 hourly), latitude (sorted into 2° bins), and month. The peak intensity is defined on the basis of the depth of the cyclone in sea level pressure, that is, the difference in sea level pressure between the center and the outermost closed pressure contour (e.g., Rudeva and Gulev 2011; Polly and Rossow 2016).

Figure 9a shows that the overall distribution of 6-hourly cyclones has a maximum number of cases at peak intensity and relatively fewer cases before and after peak. This is caused in part by considering only cyclones over the oceans, which removes from the database early or late stages when they occur over land, in part by removing cyclones in their dissipative phase when occurring poleward of 60°N/S, and in part by the variability in cyclone duration, causing some to have a relatively short onset or dissipative phase. Figure 9a indicates a slight tendency for the *CloudSat*-sampled ETC subset to have more cyclones at peak and fewer prior and after peak than do the other two datasets. Rudeva and Gulev (2011)

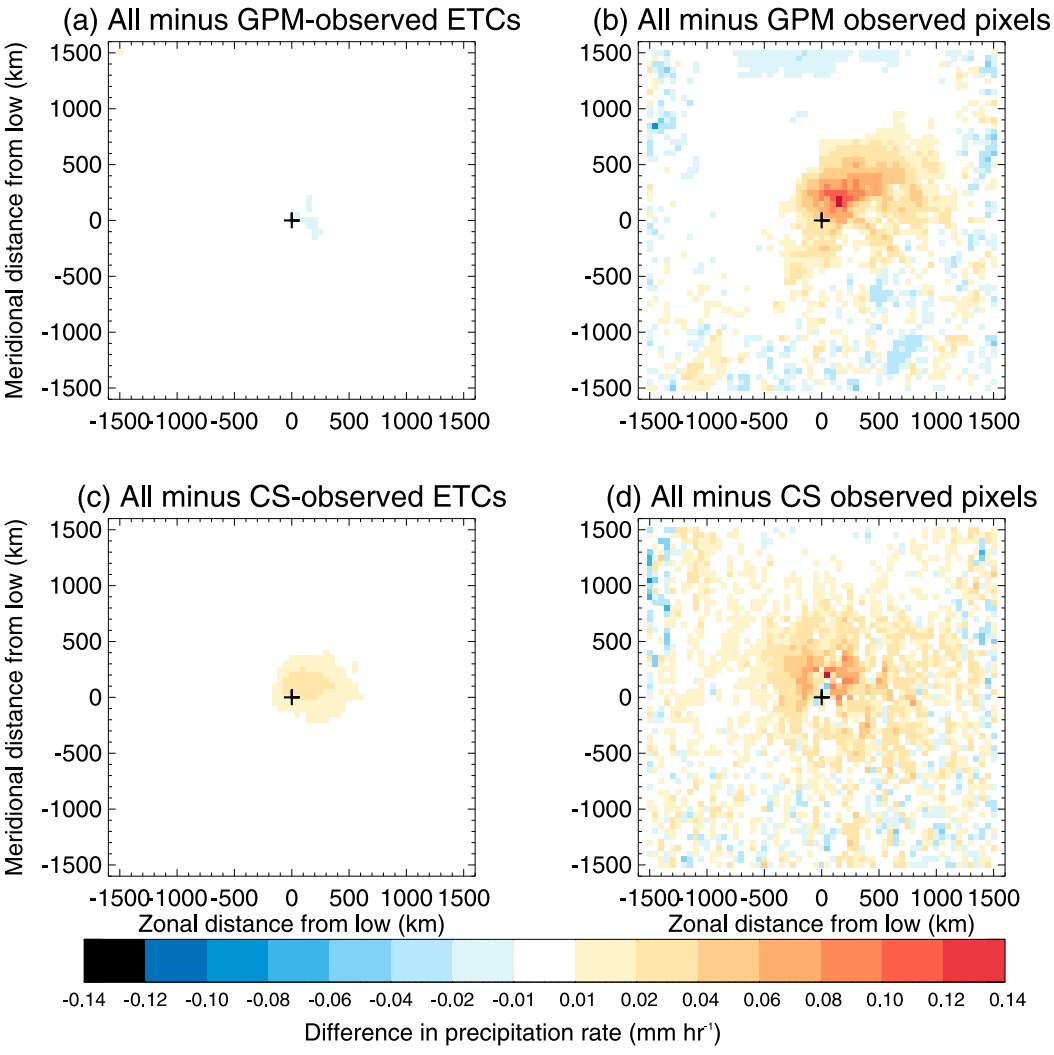

FIG. 8. Difference in cyclone-centered MERRA-2 precipitation composites (a) between the mean for all cyclones and the mean for cyclones sampled by GPM, (b) between the mean for all pixels in the cyclones and the mean for the pixels sampled by GPM, (c) between the mean for all cyclones and the mean for *CloudSat*-sampled cyclones, and (d) between the mean for all pixels in the cyclones and the mean for the *CloudSat*-sampled pixels.

find a peak in precipitation in the early stages of the cyclones and a rapid decrease as the cyclones intensify and then decay. Therefore one would expect the larger number of cyclones in the early stages for IMERG and GPM-CMB to be balanced by the larger number in the dissipation phase. Consequently, these slight variations in the cyclones' age distribution should not have a significant effect on the composites.

Figure 9b indicates a tendency for *CloudSat* to sample fewer SH and more NH cyclones than the other two datasets. This might bias the composite of *CloudSat* precipitation toward higher precipitation rates because a previous study found greater precipitation rates in NH cyclones than in SH cyclones (Naud et al. 2012). Although this might partly explain the differences between *CloudSat* and GPM-CMB, it is likely not the main reason for the difference between *CloudSat* and IMERG. The difference in zonal distribution of the cyclones is also very small in Fig. 9b. Thus, the differences in the composites among the three datasets are probably not caused by differences in the sampling locations of the cyclones.

Figure 9c shows the monthly distribution of extratropical cyclones, indicating relatively more cyclones in May and June for IMERG and relatively fewer January and February cyclones for GPM-CMB because of their period of observations. The distribution is fairly flat for *CloudSat*. There are relatively small seasonal variations in the SH, but they are large in the NH (e.g., Naud et al. 2015), and therefore monthly variations in the composites

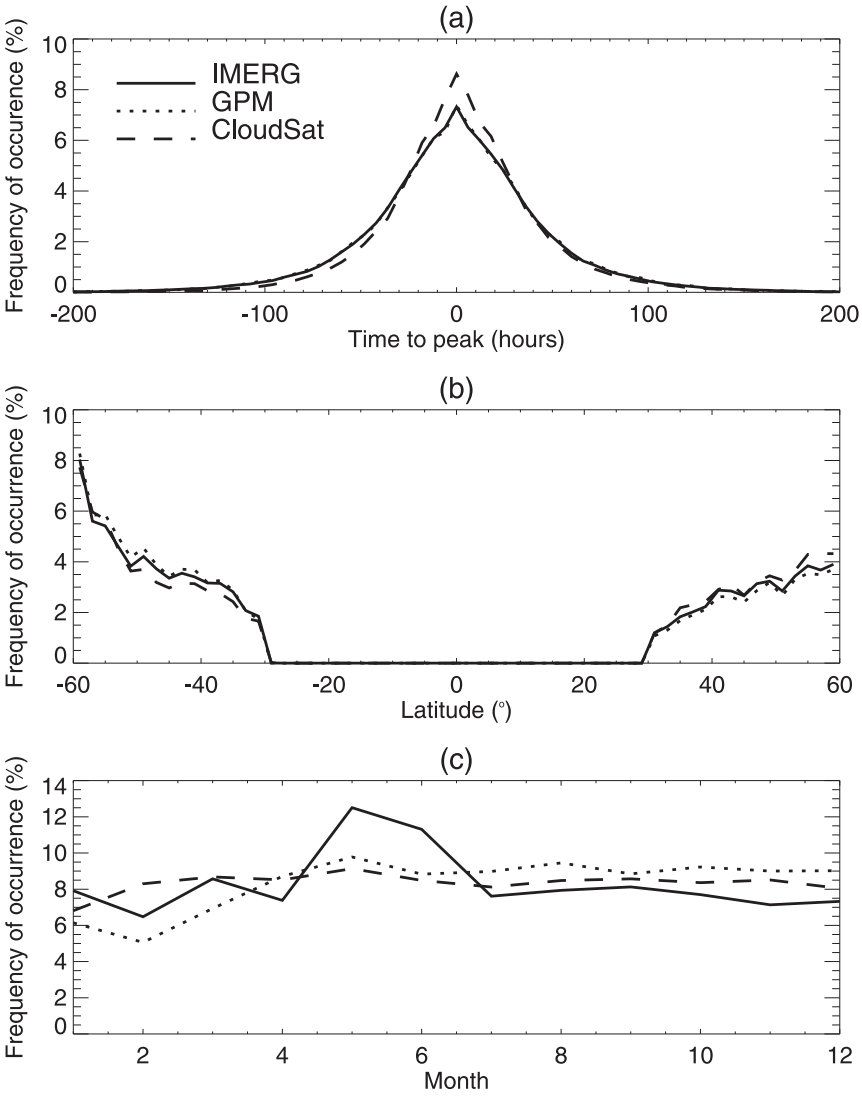

FIG. 9. Frequency of occurrence of extratropical cyclones observed by IMERG (solid lines), GPM-CMB Ka + Ku + GMI (dotted lines), and *CloudSat* (dashed lines) as a function of (a) time to peak, (b) latitude, and (c) month.

of precipitation might be influenced by the NH seasonal variations. With this in mind, we examined the variations in precipitation composites for the three datasets when subsetting into trimesters (not shown) and found that the uneven temporal distribution of GPM-CMB data alone does not explain the differences with the other datasets, whereas the larger number of cyclones in May and June does not affect the IMERG composites when compared with *CloudSat*.

Taken together, the uncertainties related to the observational setup, period length, or irregular sampling all are expected to have a much smaller impact on the composites than do the uncertainties inherent to the characteristics of the observations themselves. This result suggests that the differences observed in Fig. 5 are related to differing instrumental/retrieval sensitivities amongst the datasets rather than to sampling issues, even though the up to 0.14 mm h^{-1} sampling impact revealed in Fig. 8 might affect some of the results. Therefore, to better document the conditions that might affect each of the dataset's sensitivities, we next explore the impact of cyclone large-scale properties on the precipitation composites.

d. Sensitivity to large-scale environment

Pfahl and Sprenger (2016) and Yettella and Kay (2017) recently examined the sensitivity of precipitation in extratropical cyclones to changes in the environmental

conditions. Both studies find a strong correlation between changes in precipitation and changes in environmental moisture amounts. Therefore it seems appropriate to examine how the three datasets represent such a sensitivity, which not only would help to better characterize their differences but would also help to better constrain model evaluations.

For this, we examine the sensitivity of the composites to the mean precipitable water (PW) in the cyclone area. We subset the cyclones for each precipitation dataset into three categories on the basis of the cyclone-averaged PW. The cyclone averages are performed in a circular area of 1500-km radius, and the PW is obtained from the MERRA-2 reanalysis. The categories are defined on the basis of the entire cyclone population for both hemispheres in 2006–16. Low PW comprises all cyclones with mean cyclonewide PW of less than 11 mm, moderate PW between 11 and 19 mm, and large PW that is greater than 19 mm. This set of PW ranges is used for each dataset.

Figure 10 shows the cyclone-centered composites of precipitation for all three PW categories, using IMERG, *CloudSat*, and GPM-CMB, respectively. All three datasets show that precipitation in the cyclones is sensitive to PW, consistent with previous work with AMSR data (Field and Wood 2007). The area near the center with maximum precipitation (e.g., Fig. 2) shows an increase in precipitation rates as PW increases (in excess of $2\,\mathrm{mm\,h^{-1}}$ difference), and so does the polar half of the cyclones (but with much smaller differences, less than $0.1\,\mathrm{mm\,h^{-1}}$). It is interesting to note that, in the far corner of the eastern-equatorward quadrant, and in contrast with the warm-frontal region, cyclones with low PW tend to have slightly larger precipitation rates (up to $+0.6\,\mathrm{mm\,h^{-1}}$ difference) than cyclones with larger PW. Changes in this quadrant might be related to previous observations that larger PW in cyclones tends to be accompanied by a transition from stratiform to convective clouds and precipitation, causing larger intensities but also lower frequency of occurrence and coverage (Naud et al. 2015). Nonetheless, the first-order relationship is that greater PW means more precipitation. In recognition of this first-order dependency of precipitation on PW, the GPROF algorithm (Kummerow et al. 2015), which produces passive microwave precipitation rates that are ingested into IMERG, categorizes the Bayesian retrievals on the basis of PW.

Despite the overall agreement in PW sensitivity across the three datasets, *CloudSat* stands out because it shows larger precipitation in the moderate PW range. The issue of total attenuation for *CloudSat* retrievals probably explains the decrease in precipitation rate at the cyclone center between the moderate and large PW categories. GPM-CMB and IMERG both show a monotonic increase in composite precipitation versus PW, and this consistency gives more confidence in the idea that *CloudSat* for large PW is missing precipitation because of attenuation.

The relative difference between GPM-CMB and IMERG increases as PW increases, indicating a possible relationship between PW and retrieval bias for GPM-CMB. The reason for this behavior is unclear because attenuation is not expected to be significant for the Ku-band radar. It is possible, however, that some of the precipitation unreported by the GPM-CMB is shallow and obscured by ground clutter. It is also possible that the raindrops in the categories affected by this underestimation are smaller than what is assumed in the default electromagnetic-scattering lookup tables used by the GPM-CMB algorithm, and thus the adjustment processes (cf. Grecu et al. 2016) are not effective.

Differences between *CloudSat* and IMERG revealed in Fig. 10 suggest that the agreement between the two datasets for the composite of all cyclones (Figs. 2d and 3a) may be the result of compensating biases. IMERG reports less precipitation than *CloudSat* in the warm sector for both low and moderate PW and then balances out these biases by having more precipitation than *CloudSat* in the high PW cases.

The PW-sorting analysis provides utility to multiple different efforts. These differing sensitivities to large-scale environments provide information to help retrieval algorithm developers determine on which aspects of the algorithm to focus. Furthermore, these tests could be used for verification of future iterations of the retrievals. In the context of model evaluation, these results can help to further constrain the cyclone behavior. For relatively dry environments (low-PW categories), because of their agreement and the well-characterized performance of *CloudSat*, all three datasets could be used to provide bounds on the precipitation distribution for comparison with models. For the moderate-PW environments, *CloudSat* might be the most accurate while the other two datasets offer a lower bound on what precipitation might be. For large-PW categories, the IMERG product probably is the most accurate while GPM-CMB or *CloudSat* provide the lower bound, but additional work is required to determine whether IMERG (which, at high latitudes, is not exclusively calibrated on radar retrievals) is not biased for this category.

PW-sorting analyses also help in understanding seasonal variations in the composites from the three datasets. For the seasonal analysis, December–February (DJF), March–May (MAM), June–August (JJA), and September–November (SON) composites are generated

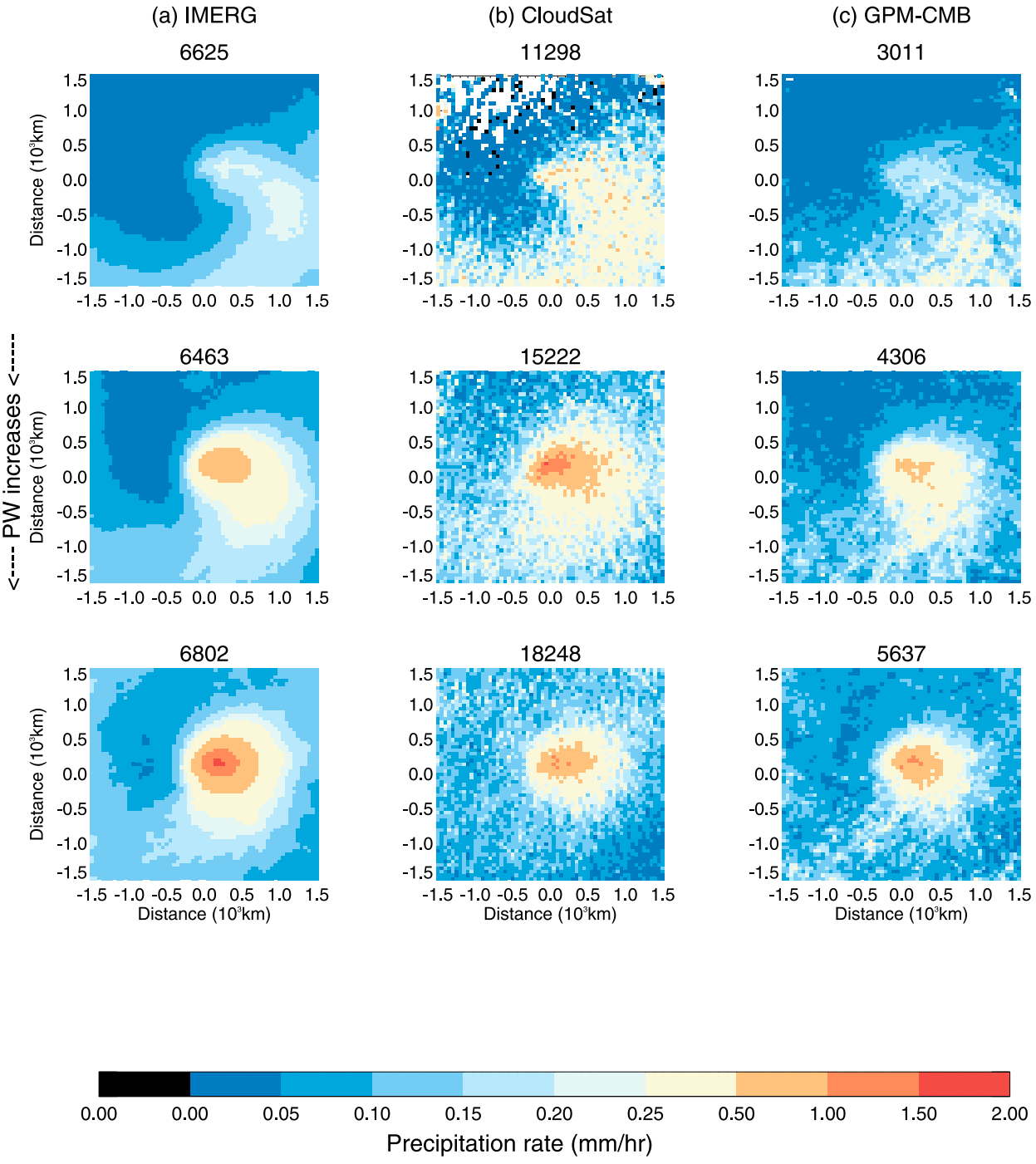

FIG. 10. Cyclone-centered composites of (a) IMERG, (b) *CloudSat*, and (c) GPM-CMB precipitation rates as a function of cyclone area-averaged PW for (top) PW < 11 mm, (middle) 11 < PW < 19 mm, and (bottom) PW > 19 mm. The numbers at the top of each plot represent the total number of cyclones included in each composite.

for NH cyclones (Fig. 11) and SH cyclones (Fig. 12) separately. For all datasets, the seasonal cycle is stronger in the NH than in the SH. The season-to-season differences are not all consistent, however. Here, we focus on the warm-frontal precipitation near the cyclone center. In the NH, IMERG and GPM-CMB have stronger precipitation rates in JJA and SON (Fig. 11). For *CloudSat*, the larger precipitation rates occur in SON and DJF. From the PW results, we interpret these differences as *CloudSat* being negatively biased (low) in

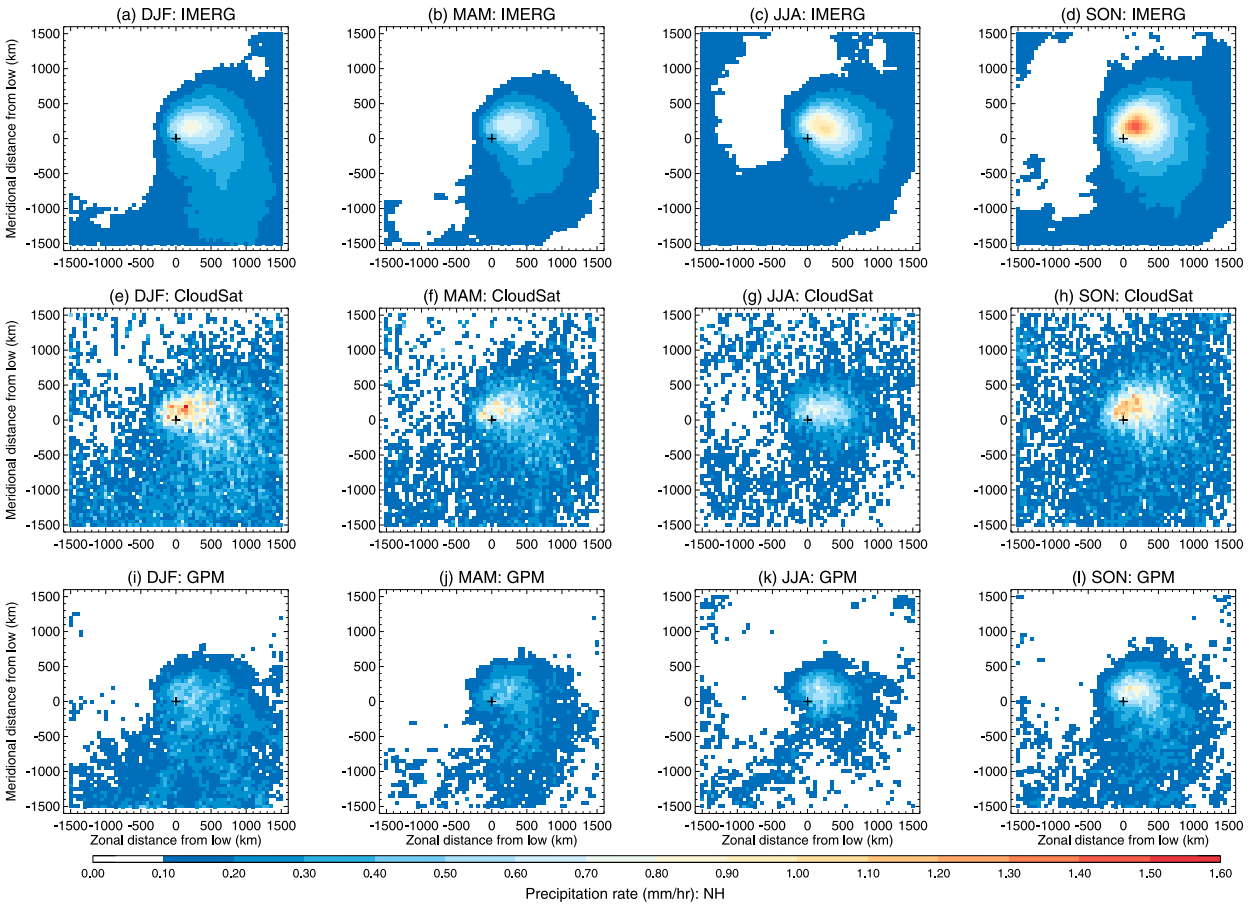

FIG. 11. Cyclone-centered composites of total precipitation for the NH for (a)–(d) IMERG, (e)–(h) *CloudSat*, and (i)–(l) GPM Ka + Ku + GMI for the (left) DJF, (left center) MAM, (right center) JJA, and (right) SON seasons.

JJA, the warmest (and highest PW) season in the NH. It is interesting to note that, despite the disparities among the three datasets, all three suggest an increase in precipitation at the center of the cyclones from JJA to SON. In the SH, the difference between IMERG and *CloudSat* is smaller in SH summer (Figs. 12a,e), presumably because the SH cyclones are dryer than their NH counterparts (Naud et al. 2012). In both hemispheres, IMERG reports lower precipitation rates at the center and elsewhere in winter and spring than does *CloudSat*, consistent with the lower rates in the low- and moderate-PW categories.

5. Conclusions

Using a database of cyclone locations over the midlatitude oceans, we constructed cyclone-centered composites of precipitation from multiple sources. Large differences in precipitation are found when comparing the different products. On average for all cyclones, IMERG and *CloudSat* precipitation in extratropical cyclones is larger than that for the other observational datasets tested here, and AMSR-E and GPCP-1DD precipitation provides the lowest composite average precipitation rates. Two reanalyses, ERA-Interim and MERRA-2, produce precipitation composites within the observational range. When compared with IMERG or *CloudSat*, GPM-CMB Ka + Ku + GMI tends to detect precipitation slightly less often and predicts lower precipitation rates, but it has higher composite precipitation values than the Ku + GMI product does.

The sensitivity of the composites to the spatial and temporal sampling of the precipitation is examined. Uncertainties related to the time period of data availability are less than 0.06 mm h^{-1}. The largest uncertainty in precipitation related to the spatial sampling is found to be caused by the irregular spatial coverage of the cyclone region by satellites with small swath widths, and it can reach up to 0.14 mm h^{-1}. In focusing on GPM-CMB Ka + Ku + GMI, IMERG, and *CloudSat*, we find larger differences related to the datasets themselves. IMERG reports precipitation more often than the other two

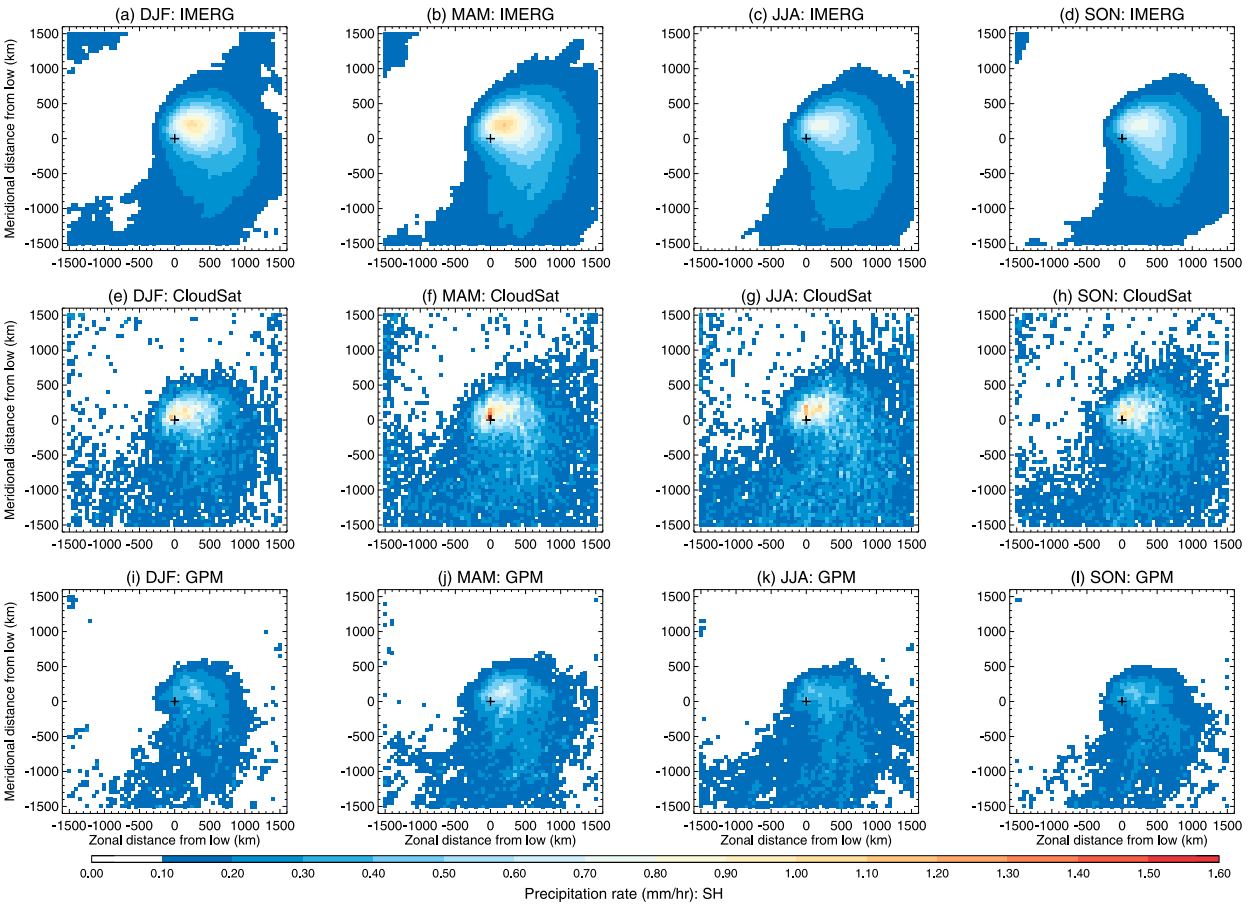

FIG. 12. As in Fig. 11, but for the SH.

datasets, and GPM-CMB reports less. GPM-CMB also detects light or large precipitation rates less often than the other two datasets, and *CloudSat* tends to underreport moderate precipitation rates relative to the other two datasets. Some of these differences can be explained by known issues with the instruments and retrieval techniques. The GPM-CMB known issue of contamination by ground clutter and low sensitivity to snow might explain lower precipitation rates than those of the other datasets. *CloudSat* issues when large precipitation rates cause radar attenuation might explain lower precipitation rates near the cyclone center than those of the other datasets in humid environments.

Therefore, these different platforms provide a *range* of observed precipitation in extratropical cyclones, and this range should be taken into account when using these composites for evaluation of GCMs. For use of cyclone-centered means near the center (±500 km) and within a wider area (±1500 km), Table 2 summarizes the results in a more quantitative fashion and provides the expected range for the datasets examined here. Collectively these different datasets provide information on the distribution of precipitation in extratropical cyclones and its sensitivity to environmental conditions:

1) Over the oceans, there is very little surface precipitation on the polar side of the cyclones, especially in the western quadrant.
2) Light precipitation dominates in the equatorward half of the cyclones, in particular in the post-cold-frontal region, that is, in the western-equatorward quadrant.
3) Heavy and moderate precipitation rates are found in the warm conveyor belt and warm-frontal regions.

Our work provides an exhaustive examination of the datasets that are at our disposal for helping to understand extratropical cyclones and their representation in GCMs. Overall, our results suggest that in fairly dry environments *CloudSat*-based composites might be more realistic than IMERG or GPM-CMB and that IMERG is more reliable in wet environments. Consequently, cyclone-centered precipitation in winter or in the SH regardless of season might be better described by *CloudSat* retrievals, whereas summertime NH cyclones

might be better described by IMERG. The GPM-CMB algorithm used here is currently being tested and improved, in part on the basis of these results, and it is expected that the work being carried out to reconcile the GPM-CMB and IMERG products for cyclones in the large-PW category will provide new insights into both algorithms. Therefore, our study also provides valuable information for future retrieval developments.

Acknowledgments. The GPM-CMB and GPM IMERG products were obtained from the NASA Goddard Space Flight Center Precipitation Processing System data server, the *CloudSat* products were obtained from the CloudSat Data Processing Center of the Colorado State University Cooperative Institute for Research in the Atmosphere, the AMSR-E products were obtained from the National Snow and Ice Data Center, the GPCP-1DD products were obtained from the NOAA data server (https://data.noaa.gov), the MERRA-2 products were obtained from the NASA Goddard Earth Sciences Data and Information Services Center, and the ERA-Interim products were obtained from the European Centre for Medium-Range Weather Forecasts. The MCMS extratropical-cyclone algorithm and documentation are available online (http://gcss-dime.giss.nasa.gov/mcms/). The database of cyclones with GPM-CMB and *CloudSat* coincident files and data is also available online (https://data.giss.nasa.gov/storms/obs-etc/). We are grateful to Dr. Paul Tol for providing IDL codes for color-blind-friendly color scales. Authors Naud and Booth were funded by NASA PMM Grant NNX16AD82G and by NOAA MAPP Grant NA15OAR4310094, with additional funding to Naud from NASA *CloudSat* Science Team Recompete Grant NNX13AQ33G. Author Grecu was funded by PMM Grant NNX16AD77G. Author Lebsock's work was carried out at the Jet Propulsion Laboratory, California Institute of Technology, under contract with the National Aeronautics and Space Administration through RTOP/WBS 103428/8.A.1.6.

REFERENCES

Adler, R. F., and Coauthors, 2003: The version 2 Global Precipitation Climatology Project (GPCP) Monthly Precipitation Analysis (1979–present). *J. Hydrometeor.*, **4**, 1147–1167, https://doi.org/10.1175/1525-7541(2003)004<1147:TVGPCP>2.0.CO;2.

Bauer, M., and A. D. Del Genio, 2006: Composite analysis of winter cyclones in a GCM: Influence on climatological humidity. *J. Climate*, **19**, 1652–1672, https://doi.org/10.1175/JCLI3690.1.

——, G. Tselioudis, and W. B. Rossow, 2016: A new climatology for investigating storm influences in and on the extratropics. *J. Appl. Meteor. Climatol.*, **55**, 1287–1303, https://doi.org/10.1175/JAMC-D-15-0245.1.

Behrangi, A., M. Lebsock, S. Wong, and B. Lambrigtsen, 2012: On the quantification of oceanic rainfall using spaceborne sensors. *J. Geophys. Res.*, **117**, D20105, https://doi.org/10.1029/2012JD017979.

——, G. Stephens, R. F. Adler, G. J. Huffman, B. Lambrigtsen, and M. Lebsock, 2014: An update on the oceanic precipitation rate and its zonal distribution in light of advanced observations from space. *J. Climate*, **27**, 3957–3965, https://doi.org/10.1175/JCLI-D-13-00679.1.

Casella, D., G. Panegrossi, P. Sanò, A. C. Marra, S. Dietrich, B. T. Johnson, and M. S. Kulie, 2017: Evaluation of the GPM–DPR snowfall detection capability: Comparison with *CloudSat*-CPR. *Atmos. Res.*, **197**, 64–75, https://doi.org/10.1016/j.atmosres.2017.06.018.

Catto, J. L., L. C. Shaffrey, and K. I. Hodges, 2010: Can climate models capture the structure of extratropical cyclones? *J. Climate*, **23**, 1621–1635, https://doi.org/10.1175/2009JCLI3318.1.

——, C. Jakob, G. Berry, and N. Nicholls, 2012: Relating global precipitation to atmospheric fronts. *Geophys. Res. Lett.*, **39**, L10805, https://doi.org/10.1029/2012GL051736.

——, ——, and N. Nicholls, 2015: Can the CMIP5 models represent winter frontal precipitation? *Geophys. Res. Lett.*, **42**, 8596–8604, https://doi.org/10.1002/2015GL066015.

Dee, D. P., and Coauthors, 2011: The ERA-Interim reanalysis: Configuration and performance of the data assimilation systems. *Quart. J. Roy. Meteor. Soc.*, **137**, 553–597, https://doi.org/10.1002/qj.828.

de Leeuw, J., J. Methven, and M. Blackburn, 2015: Evaluation of ERA-Interim reanalysis precipitation products using England and Wales observations. *Quart. J. Roy. Meteor. Soc.*, **141**, 798–806, https://doi.org/10.1002/qj.2395.

Field, P. R., and R. Wood, 2007: Precipitation and cloud structure in midlatitude cyclones. *J. Climate*, **20**, 233–254, https://doi.org/10.1175/JCLI3998.1.

——, A. Gettelman, R. Neale, R. Wood, P. J. Rasch, and H. Morrison, 2008: Midlatitude cyclone compositing to constrain climate model behavior using satellite observations. *J. Climate*, **21**, 5887–5903, https://doi.org/10.1175/2008JCLI2235.1.

——, A. Bodas-Salcedo, and M. E. Brooks, 2011: Using model analysis and satellite data to assess cloud and precipitation in midlatitude cyclones. *Quart. J. Roy. Meteor. Soc.*, **137**, 1501–1515, https://doi.org/10.1002/qj.858.

Gelaro, R., and Coauthors, 2017: The Modern-Era Retrospective Analysis for Research and Applications, version 2 (MERRA-2). *J. Climate*, **30**, 5419–5454, https://doi.org/10.1175/JCLI-D-16-0758.1.

Govekar, P. D., C. Jakob, and J. Catto, 2014: The relationship between clouds and dynamics in Southern Hemisphere extratropical cyclones in the real world and a climate model. *J. Geophys. Res. Atmos.*, **119**, 6609–6628, https://doi.org/10.1002/2013JD020699.

Grecu, M., W. S. Olson, S. J. Munchak, S. Ringerud, L. Liao, Z. Haddad, B. L. Kelley, and S. F. McLaughlin, 2016: The GPM combined algorithm. *J. Atmos. Oceanic Technol.*, **33**, 2225–2245, https://doi.org/10.1175/JTECH-D-16-0019.1.

Hawcroft, M. K., L. C. Shaffrey, K. I. Hodeges, and H. F. Dacre, 2012: How much Northern Hemisphere precipitation is associated with extratropical cyclones? *Geophys. Res. Lett.*, **39**, L24809, https://doi.org/10.1029/2012GL053866.

——, ——, K. I. Hodges, and H. F. Dacre, 2016: Can climate models represent the precipitation associated with extratropical cyclones? *Climate Dyn.*, **47**, 679–695, https://doi.org/10.1007/s00382-015-2863-z.

Haynes, J. M., T. S. L'Ecuyer, G. L. Stephens, S. D. Miller, C. Mitrscu, N. B. Wood, and S. Tanelli, 2009: Rainfall retrieval over the ocean with spaceborne W-band radar. *J. Geophys. Res.*, **114**, D00A22, https://doi.org/10.1029/2008JD009973.

Hou, A. Y., and Coauthors, 2014: The Global Precipitation Measurement mission. *Bull. Amer. Meteor. Soc.*, **95**, 701–722, https://doi.org/10.1175/BAMS-D-13-00164.1.

Huffman, G. J., R. F. Adler, M. Morrissey, D. T. Bolvin, S. Curtis, R. Joyce, B. McGavock, and J. Susskind, 2001: Global precipitation at one-degree daily resolution from multisatellite observations. *J. Hydrometeor.*, **2**, 36–50, https://doi.org/10.1175/1525-7541(2001)002<0036:GPAODD>2.0.CO;2.

——, and Coauthors, 2017: NASA Global Precipitation Measurement (GPM) Integrated Multi-satellite Retrievals for GPM (IMERG). Algorithm Theoretical Basis Doc. (version 4.6), 32 pp., https://pmm.nasa.gov/sites/default/files/document_files/IMERG_ATBD_V4.6.pdf.

Kawanishi, T., and Coauthors, 2003: The Advanced Microwave Scanning Radiometer for the Earth Observing System (AMSR-E), NASDA's contribution to the EOS for global energy and water cycle studies. *IEEE Trans. Geosci. Remote Sens.*, **41**, 184–194, https://doi.org/10.1109/TGRS.2002.808331.

Klein, S. A., and C. Jakob, 1999: Validation and sensitivities of frontal clouds simulated by the ECMWF model. *Mon. Wea. Rev.*, **127**, 2514–2531, https://doi.org/10.1175/1520-0493(1999)127<2514:VASOFC>2.0.CO;2.

Kummerow C., W. Barnes, T. Kozu, J. Shiue, and J. Simpson, 1998: The Tropical Rainfall Measuring Mission (TRMM) sensor package. *J. Atmos. Oceanic Technol.*, **15**, 809–817, https://doi.org/10.1175/1520-0426(1998)015<0809:TTRMMT>2.0.CO;2.

Kummerow, C., and Coauthors, 2000: The status of the Tropical Rainfall Measuring Mission (TRMM) after two years in orbit. *J. Appl. Meteor.*, **39**, 1965–1982, https://doi.org/10.1175/1520-0450(2001)040<1965:TSOTTR>2.0.CO;2.

——, S. Ringerud, J. Crook, D. Randel, and W. Berg, 2011: An observationally generated a priori database for microwave rainfall retrievals. *J. Atmos. Oceanic Technol.*, **28**, 113–130, https://doi.org/10.1175/2010JTECHA1468.1.

——, D. L. Randel, M. Kulie, N.-Y. Wang, R. Ferraro, S. J. Munchak, and V. Petkovic, 2015: The evolution of the Goddard profiling algorithm to a fully parametric scheme. *J. Atmos. Oceanic Technol.*, **32**, 2265–2280, https://doi.org/10.1175/JTECH-D-15-0039.1.

Lau, N.-C., and M. W. Crane, 1995: A satellite view of the synoptic-scale organization of cloud properties in midlatitude and tropical circulation systems. *Mon. Wea. Rev.*, **123**, 1984–2006, https://doi.org/10.1175/1520-0493(1995)123<1984:ASVOTS>2.0.CO;2.

Naud, C. M., A. D. Del Genio, and M. Bauer, 2006: Observational constraints on the cloud thermodynamic phase in midlatitude storms. *J. Climate*, **19**, 5273–5288, https://doi.org/10.1175/JCLI3919.1.

——, ——, ——, and W. Kovari, 2010: Cloud vertical distribution across warm and cold fronts in *CloudSat–CALIPSO* data and a general circulation model. *J. Climate*, **23**, 3397–3415, https://doi.org/10.1175/2010JCLI3282.1.

——, D. J. Posselt, and S. C. van den Heever, 2012: Observational analysis of cloud and precipitation in midlatitude cyclones: Northern versus Southern Hemisphere warm fronts. *J. Climate*, **25**, 5135–5151, https://doi.org/10.1175/JCLI-D-11-00569.1.

——, ——, and ——, 2015: A *CloudSat–CALIPSO* view of cloud and precipitation properties across cold fronts over the global oceans. *J. Climate*, **28**, 6743–6762, https://doi.org/10.1175/JCLI-D-15-0052.1.

Pfahl, S., and M. Sprenger, 2016: On the relationship between extratropical cyclone precipitation and intensity. *Geophys. Res. Lett.*, **43**, 1752–1758, https://doi.org/10.1002/2016GL068018.

Polly, J. B., and W. B. Rossow, 2016: Cloud radiative effects and precipitation in extratropical cyclones. *J. Climate*, **29**, 6483–6507, https://doi.org/10.1175/JCLI-D-15-0857.1.

Reichle, R. H., Q. Liu, R. D. Koster, C. S. Draper, S. P. P. Mahanama, and G. S. Partyka, 2017: Land surface precipitation in MERRA-2. *J. Climate*, **30**, 1643–1664, https://doi.org/10.1175/JCLI-D-16-0570.1.

Rudeva, I., and S. K. Gulev, 2011: Composite analysis of north Atlantic extratropical cyclones in NCEP–NCAR reanalysis data. *Mon. Wea. Rev.*, **139**, 1419–1446, https://doi.org/10.1175/2010MWR3294.1.

Simpson, J. R., R. F. Adler, and G. R. North, 1988: A proposed Tropical Rainfall Measuring Mission (TRMM) satellite. *Bull. Amer. Meteor. Soc.*, **69**, 278–295, https://doi.org/10.1175/1520-0477(1988)069<0278:APTRMM>2.0.CO;2.

Skofronick-Jackson, G., and Coauthors, 2017: The Global Precipitation Measurement (GPM) mission for science and society. *Bull. Amer. Meteor. Soc.*, **98**, 1679–1695, https://doi.org/10.1175/BAMS-D-15-00306.1.

Stephens, G. L., and Coauthors, 2002: The *CloudSat* mission and the A-Train: A new dimension to space-based observations of clouds and precipitation. *Bull. Amer. Meteor. Soc.*, **83**, 1771–1790, https://doi.org/10.1175/BAMS-83-12-1771.

——, and Coauthors, 2010: Dreary state of precipitation in global models. *J. Geophys. Res.*, **115**, D24211, https://doi.org/10.1029/2010JD014532.

Tanelli, S., S. L. Durden, E. Im, K. S. Pak, D. G. Reinke, P. Partain, J. M. Haynes, and R. T. Marchand, 2008: *CloudSat*'s cloud profiling radar after two years in orbit: Performance, calibration, and processing. *IEEE Trans. Geosci. Remote Sens.*, **46**, 3560–3573, https://doi.org/10.1109/TGRS.2008.2002030.

Yettella, V., and J. E. Kay, 2017: How will precipitation change in extratropical cyclones as the planet warms? Insights from a large initial condition climate model ensemble. *Climate Dyn.*, **49**, 1765–1781, https://doi.org/10.1007/s00382-016-3410-2.